


Spin-Blockade Spectroscopy of Si/Si-Ge Quantum Dots

A.M. Jones,^{*} E.J. Pritchett, E.H. Chen, T.E. Keating, R.W. Andrews, J.Z. Blumoff,
L.A. De Lorenzo, K. Eng, S.D. Ha, A.A. Kiselev, S.M. Meenehan, S.T. Merkel, J.A. Wright, L.F. Edge,
R.S. Ross, M.T. Rakher, M.G. Borselli, and A. Hunter
HRL Laboratories, LLC, 3011 Malibu Canyon Road, Malibu, California 90265, USA

 (Received 29 September 2018; revised manuscript received 11 June 2019; published 15 July 2019)

We implement a technique for measuring the singlet-triplet energy splitting responsible for spin-to-charge conversion in semiconductor quantum dots. This method, which requires fast, single-shot charge measurement, reliably extracts both large and small splittings. We perform this technique on an undoped, accumulation-mode Si/Si-Ge triple-quantum dot and find that the measured splitting varies smoothly as a function of confinement gate biases. Not only does this demonstration prove the value of having an *in situ* excited-state measurement technique as part of a standard tune-up procedure, but it also suggests that in typical Si/Si-Ge quantum-dot devices, spin blockade can be limited by lateral orbital excitation energies rather than valley splitting.

DOI: [10.1103/PhysRevApplied.12.014026](https://doi.org/10.1103/PhysRevApplied.12.014026)

I. INTRODUCTION

Qubits based on electrons confined in silicon quantum dots (QDs) benefit from the advantages inherent in many semiconductor platforms: fast control, small form factors, and established fabrication methods. Moreover, mitigation of a dominant decoherence pathway—interactions with nonzero-spin nuclei—is possible with isotopic enhancement [1]. These advantages have led to key demonstrations, including extended coherence [2–4] as well as fast, accurate control via a number of techniques including tunnel-barrier modulation [5,6], electron spin resonance [7–9], and induced spin-orbit coupling [10]. Recently, one-qubit randomized benchmarking [7,11,12], two-qubit randomized benchmarking [13], and two-qubit entangling sequences [11,14,15] have been demonstrated with Si-based qubits.

Many quantum-dot-based qubits rely on the conversion of electron spin states, which preserve quantum information by interacting weakly with their electrical environment, to charge states for control and measurement. In exchange-based schemes, distinct spin states of two interacting electrons (spin singlets and spin triplets) are converted into distinguishable charge states utilizing the well-established principles of Pauli spin blockade (SB) [16]. The robustness of SB relies on the energy separation between the ground-singlet and ground-triplet levels of two electrons occupying the same dot, denoted here as Δ_{SB} . This energy limits state measurement and preparation fidelities by setting the range over which one can

achieve spin-to-charge conversion and the accuracy with which one can initialize a ground-state singlet in a system at finite temperature [17].

Establishing what limits Δ_{SB} in Si QDs is crucial for qubit design. While orbital excitation energies are, in principle, easily manipulated by changing confining potentials with gate biases, the maximum attainable Δ_{SB} is conventionally thought to be limited by valley splitting, the energy splitting between the two lowest-lying quantized states originating from conduction-band valleys of bulk, tensile strained silicon [18]. Two-electron orbital energies are determined by the strength and symmetry of in-plane confinement [16,19], whereas valley splittings are determined primarily by the details of out-of-plane electron confinement, a challenge that has inspired many theoretical and engineering efforts [18,20–22]. Numerous techniques have been used to estimate the magnitude of valley splitting in Si/Si-Ge quantum dots, including photon-assisted tunneling [23], cavity coupling [24], Landau-Zener-Stückelberg interferometry [25], magnetotransport [22], and magnetospectroscopy [26,27]. However, the results of these techniques may not accurately measure Δ_{SB} as they probe length scales not generally relevant to QD electrons, require the application of additional electromagnetic fields, or use biasing configurations different from nominal operation. These conditions impede a direct translation of the measured energies to qubit performance.

In this paper, we describe an excited-state spectroscopy technique that leverages recent developments in single-shot measurement of spins [3,9,28–31] to directly measure Δ_{SB} . The utility of this method lies in its ability to not only extract this energy *in situ* for large splittings [28,32], but

^{*}amjones@hrl.com

also in the limit where Δ_{SB} is on par with thermal energies and/or interdot tunnel couplings, and to do so without relying on a detailed physical model or the addition of controls (e.g., large magnetic fields [26,27,33]) beyond those normally required to operate exchange-only quantum-dot qubits.

We discuss the requirements placed on our measurement system to perform this technique, which is fundamentally limited by the fidelity of single-shot state discrimination and T_1 relaxation rates. We then demonstrate this technique on a Si/Si-Ge double dot and find Δ_{SB} to be highly tunable and smoothly varying with bias voltages, suggesting that Δ_{SB} in this device could be limited by orbital confinement energy rather than valley splitting [33–35]. Both the establishment of a reliable method for *in situ* excited-state spectroscopy and the identification of limitations to device performance should be relevant to many QD architectures.

II. METHODS

A. Spin-to-charge conversion

We measure an accumulation-mode, Si/Si-Ge triple dot [Fig. 1(a)], which is similar to other devices [36–40] that have demonstrated both a scalable platform for trapping many electrons [41] and universal qubit control [3,5]. Building on our previous experience [37,42], electrons are confined in a tensile-strained Si quantum well, embedded in a strain-relaxed, undoped Si-Ge alloy. Lateral confinement is provided by two types of overlapping Al gates separated by atomic layer deposition oxides: large field gates that prevent the accumulation of electrons in undesirable locations [outlined in Fig. 1(a)] and small gates for controlling individual dots. Quantum dots are defined under the “plunger” gates labeled $P1$, $P2$, and $P3$ and are loaded from electron reservoirs under the “bath” gates $B1$ and $B2$. Tunneling from the baths to the dots is mediated by the “tunnel” gates $T1$ and $T2$, and interdot tunnel coupling is controlled by the “exchange” gates $X1$ and $X2$. Bound electrons capacitively couple to the “measure” dot M , with each charge configuration affecting the measured conductance as seen in Fig. 1(b). Gate biases provide control of the triple dot through two mechanisms: a linear response in the chemical potentials, which can sensitively calibrate away any residual charge disorder, and an exponential response in tunnel coupling, which allows fast control with large on:off ratios and ultimately facilitates high-performance quantum gates.

Spin-to-charge conversion (SCC), by which two-electron spin states are converted into distinct charge states, occurs at biases where two-electron number-conserving charge states are nearly degenerate, e.g., bottom right: $(2,0)$ – $(1,1)$ and top left: $(0,2)$ – $(1,1)$ of Fig. 1(b) [16,43]. As dictated by the Pauli exclusion principle, the two-electron spin-symmetric triplet must be antisymmetric in some other degree of freedom. In silicon, this can be

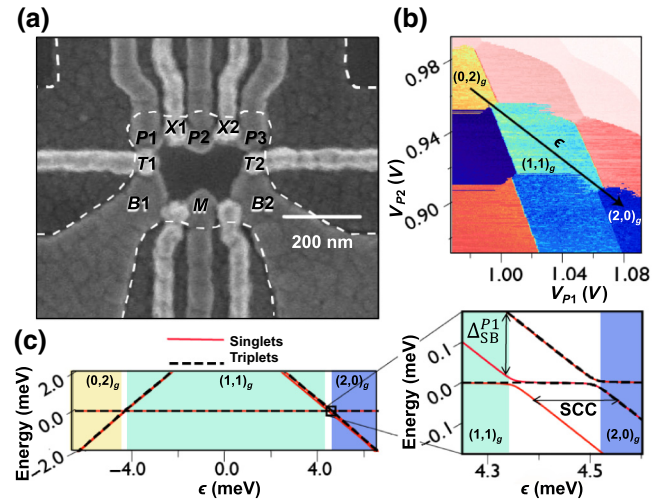


FIG. 1. Device scanning electron micrograph, charge stability, and energy level schematic. (a) Scanning electron micrograph of a triple-dot device defined by gates $P1$, $P2$, $P3$, with nearby quantum dot electrometer, M . Outline indicates large-area field gate. (b) Charge stability map versus applied voltage on gates $P1$ and $P2$, with color indicating measured current through charge sensor M . (c) Energy levels versus detuning, ϵ , of a two-electron Fermi-Hubbard model for spin singlet (solid) and triplet (dashed) states.

provided by valley, orbital excitation, or some hybridization of the two [34]. The ground-singlet to ground-triplet energy splitting of two electrons occupying dot P_i , denoted $\Delta_{SB}^{P_i}$, determines the range of detunings that support SCC, i.e., biases at which the ground triplet remains in the $(1,1)$ charge state while the ground singlet occupies a single QD [see Fig. 1(c)]. These distinct charge states result in different electrostatic potentials at the measure dot, leading to measurably different conductances at this charge sensor [37].

Our technique measures $\Delta_{SB}^{P_i}$ by analyzing single-shot current values as singlet or triplet mixed states are swept adiabatically through detunings that support spin-to-charge conversion. This involves a four-step pulse sequence: (1) state preparation, (2) spin dephasing, (3) measurement near SCC, and (4) a final charge reference measurement. In step (1) we prepare a spin singlet by biasing near the $(1,0)$ – $(2,0)$ charge boundary where fast cotunneling processes quickly relax $(2,0)$ triplets to $(2,0)$ singlets. For step (2), to prepare a mixed state, we adiabatically traverse the $(2,0)$ – $(1,1)$ anticrossing and rapidly pulse to the center of the $(1,1)$ cell [center of Fig. 1(b)]. Then the spin singlet is allowed to dephase in a bath of fluctuating, nonzero-spin nuclei for $10 \mu\text{s}$, which is long compared to the measured $T_2^* \simeq 2 \mu\text{s}$ in this 800 ppm ^{29}Si device. In step (3) the resulting mixed state is rapidly biased back near the $(1,1)$ – $(2,0)$ anticrossing, then adiabatically ramped to a measurement point, which is swept through detunings near and including SCC. A second measurement (4) is performed deep within the

(2,0) cell and subtracted from the first to remove the effects of low-frequency charge noise. This sequence is very similar to those used for standard quantum measurements when operating the device as a singlet-triplet qubit [3]. However, high-fidelity state preparation in step (1) is unnecessary as the remaining steps work identically for a mixture of ground singlets and triplets.

B. Single-shot measurement

Measuring capacitive shifts at the charge sensor requires a chain of cryogenic and room-temperature electronics leading to both the source and drain electrodes. Changes in charge-sensor current are detected using lock-in amplification techniques. The lock-in tone is a series of alternating square pulses from an arbitrary waveform generator at room temperature sent down the source line. This line has 10 000:1 voltage division at room temperature to mitigate voltage noise and is filtered by a commercial low-pass filter with a 120-MHz cutoff frequency. Alternating current driven through the charge sensor is converted back into voltage using an approximately 20-kOhm shunt resistor (see Fig. 2), which reduces the impedance of the high-impedance charge sensor (approximately 100 kOhm). Since the measured voltage scales linearly with the value of the shunt resistor, we increase our bandwidth by minimizing parasitic capacitance between the drain and the amplifiers, rather than by lowering the resistance. By mounting pHEMTs on standoffs located near the device [44], we achieve a capacitance of approximately 8 pF, allowing for a measurement bandwidth of 1 MHz, well above the $1/f$ corner frequency of our electronics. The voltage signal is amplified approximately 60 dB using two stages of amplification (Avago ATF-38143 pHEMTs) held at approximately 1 K and approximately 4 K. The amplified voltage is delivered using rf coaxial cables and digitized at room temperature using commercial ADCs where the lock-in tone through the charge sensor is demodulated and converted into units of conductance. Components of this measurement chain that contribute to the total noise floor of the measurement include the Johnson noise of

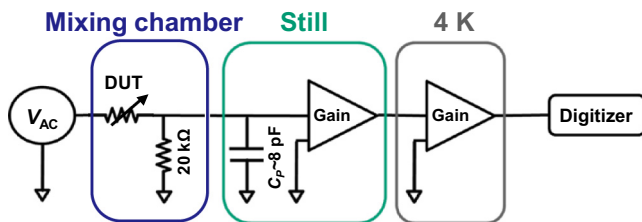


FIG. 2. Experiment measurement chain. At the output of the device under test (DUT), a 20-kOhm shunt resistor on the mixing chamber stage converts current to voltage. With approximately 8 pF of parasitic capacitance, this arrives at the first HEMT amplification stage held at approximately 1 K before passing through the second stage held at approximately 4 K.

the shunt resistor ($332 \text{ pV}/\sqrt{\text{Hz}}$ at 100 mK), shot noise ($253 \text{ pV}/\sqrt{\text{Hz}}$), and the input-referred noise of the pHEMT amplifiers (approximately $250 \text{ pV}/\sqrt{\text{Hz}}$). Integrating these sources with our measurement filter function and adding the result to the $1/f$ charge-noise contribution (3.65 pA broadening for $5 \text{ } \mu\text{V}/\sqrt{\text{Hz}}$ at 1 Hz of gate-referred noise), we calculate a total broadening of 7.7 pA.

A critical aspect of accurately resolving Δ_{SB} using our technique is the ability to perform single-shot charge measurements at timescales much shorter than singlet-triplet T_1 processes. Since measurement uncertainty scales quadratically with histogram width, σ_I , the blurring of singlet and triplet histograms caused by T_1 decay during measurement is detrimental, especially when a small Δ_{SB} and/or a high electron temperature limits SNR on fast timescales. Near the region of SCC, we typically observe $T_1 > 100 \text{ } \mu\text{s}$, while the total measurement integration time is $12.5 \text{ } \mu\text{s}$. This fast measurement time is a result of the reduced parasitic capacitance achieved by mounting cryogenic HEMTs near the device.

C. Energy scaling

In order to accurately convert the applied detuning bias voltages of step (3) in the pulse sequence to an energy scale, we incorporate both the gate lever arm strength and cross capacitance between dots P_1 and P_2 in calculating a scaling factor. While several methods for doing this have been presented elsewhere (cf. photon-assisted tunneling [45,46]), we outline our two-step process here.

First, we obtain the lever arm strength, α , of each plunger gate by fitting a charge-transition width as a function of refrigerator temperature [28]. For the P_1 and P_2 plunger gates we monitor the (1,0)–(2,0) and (3,0)–(3,1) charge transitions, respectively, chosen because of their proximity to the region of SCC and moderate tunneling rates. The measured linewidth of each transition as a function of refrigerator base temperature is shown in Fig. 3. These curves are fit to a phenomenological expression, which assumes that contributions to the linewidth stem from an incoherent sum of the measured temperature of the mixing chamber, T_{MC} , and a constant electronic “effective” temperature, T_e , as

$$\Delta V(T_{\text{MC}}) = \frac{k_B \sqrt{T_{\text{MC}}^2 + T_e^2}}{\alpha}. \quad (1)$$

Fits to the data (blue and green lines in Fig. 3) yield $\alpha_{P_1} = 0.095 \text{ eV/V}$ and $\alpha_{P_2} = 0.104 \text{ eV/V}$. The difference between α_{P_1} and α_{P_2} (9%) is much higher than the fitting error and better reflects the variation found within an ensemble of lever arm measurements. This variation is a significant source of uncertainty in converting detuning biases to energy, and consequently the magnitude of the extracted Δ_{SB} .

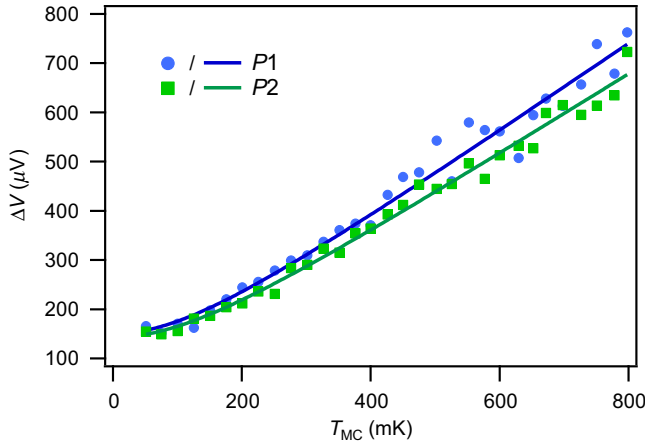


FIG. 3. Charge transition width versus refrigerator base temperature. Measured width, $\Delta V(T_{MC})$, of the $P1$ (1,0)–(2,0) (blue circles) and $P2$ (3,0)–(3,1) (green squares) charge transitions as a function of refrigerator base temperature, T_{MC} . Blue and green lines show fits to corresponding data sets to extract lever arm strength.

Second, we measure the cross capacitance of gate $P2$ on an electron loaded under $P1$ compared to the capacitance of gate $P1$ on the same electron, which we denote $G_{P1,P2}$, by measuring the slope of a $P1$ loading line with respect to bias V_{P2} . $G_{P2,P1}$ can be measured similarly. The four measured factors α_{P1} , α_{P2} , $G_{P1,P2}$, and $G_{P2,P1}$, together with the relative bias swept on gates $P2$ and $P1$ (ΔV_{P2} and ΔV_{P1} where $\Delta V_{P1} - \Delta V_{P2}$ is the detuning bias), allow us to convert the $P1$ voltage range supporting spin blockade, ΔV_{SB} , to energy:

$$\Delta_{SB} = \left| \alpha_{P1} - \alpha_{P2} \times G_{P2,P1} - \frac{\Delta V_{P2}}{\Delta V_{P1}} (\alpha_{P2} - \alpha_{P1} \times G_{P1,P2}) \right| \Delta V_{SB}. \quad (2)$$

III. RESULTS

The region of SCC is revealed as a step in the contrast of conductance between measurements at steps (2) and (4) of the applied pulse sequence, apparent in a two-dimensional sweep of the biases on $P1$ and $P2$ during the first measurement [see Fig. 4(a)]. We extract the energy Δ_{SB} by taking a line cut [marked in red in Fig. 4(a)] perpendicular to the region of SCC and repeating the pulse sequence many times at each point along this detuning axis, recording the result of each repetition. This results in a distribution of independently measured currents at each value of detuning. We bin the number of counts at a given detuning within a range of measured current values to obtain the grayscale intensity plot of Fig. 4(b), revealing two distinct branches of the transition from the higher-current (1,1) charge state to the lower-current (2,0) charge state. With

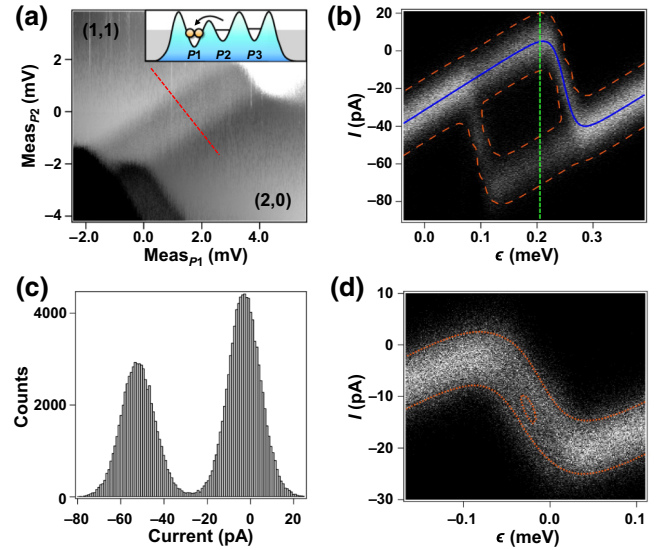


FIG. 4. Single-shot measurements of two-electron ground- and excited-state avoided crossings. (a) Charge-stability scan around the (2,0)–(1,1) avoided crossings, employing a prepare-dephase-measure pulse sequence. Grayscale contrast derives from differential measurement of current through charge sensor M. Inset: Sketch depicting the one-dimensional potential profile of dots $P1$, $P2$, and $P3$ for biasing at the figure center. Detuning from (1,1) towards (2,0) dumps both electrons (yellow circles) into $P1$. (b) 5000 single-shot measurements taken at each point along the red detuning line in (a). Vertical axis: measured current value. Horizontal axis: detuning, in meV, from a point near the (2,0)–(1,1) anticrossing. Grayscale contrast corresponds to the number of counts at each detuning and binned current value. Orange dashed lines show the contour line from the fit to Eq. (7). The blue line shows the triplet-branch profile using the form of Eq. (5). (c) 150 000 shot histogram taken at the detuning indicated by the green line in (b). (d) Data from the (2,0)–(1,1) anticrossing of a second similar device. 500 shots are taken at each detuning. Orange dashed lines show the contour line from the fit to Eq. (7).

positive detuning defined to be in the (1,1) to (2,0) direction, we ascribe the charge transition that occurs at smaller detuning to a spin-singlet state. The transition occurring at larger detuning then corresponds to a spin triplet, separated from the singlet branch by the lowest excited-state energy of both electrons occupying dot $P1$, Δ_{SB}^{P1} .

The pulse sequence can easily be modified to measure the energy splitting of dot $P2$. Since $P2$ is more isolated from the bath, state preparation must still be performed on dot $P1$, leaving steps (1) and (2), state preparation and dephasing, as before. Measurement is then performed near the region of SCC at the (0,2)–(1,1) charge boundary, with the final charge reference measurement set within the (0,2) charge cell. These slight modifications allow Δ_{SB} to be measured on two quantum dots with minimal change to the electrostatic configuration.

A. Fermi-Hubbard model

We derive our fit model from a Fermi-Hubbard model, following Ref. [47]. Near the charge boundary where we perform measurement, the system's ground state is a superposition of (1,1) and (2,0) charge states, connected by a two-electron tunnel coupling, t_c , with detuning ϵ . We assume that the electrons have a valley and/or orbital degree of freedom with excitation energy Δ_{SB} , so that the ground $|g\rangle_{20}$ and excited $|e\rangle_{20}$ states of two electrons occupying the same dot [the (2,0) charge configuration indicated by subscript] have splitting Δ_{SB} . At detunings near the region of SCC, the system's ground state is dominated by the lowest allowed energy states: $|g\rangle_{11}$ and $|g\rangle_{02}$ for spin singlets and $|g\rangle_{11}$ and $|e\rangle_{02}$ for spin triplets. $|g\rangle_{02}$ is forbidden for spin triplets by the Pauli exclusion principle. In this reduced basis, we can write the Hamiltonian as $H = H_S + H_T$ where

$$H_S \approx t_c^S (|g\rangle_{11\ 20} |g\rangle + \text{h.c.}) - \epsilon |g\rangle_{20\ 20} \langle g|, \quad (3)$$

$$H_T \approx t_c^T (|g\rangle_{11\ 20} |e\rangle + \text{h.c.}) - (\epsilon - \Delta_{SB}) |e\rangle_{20\ 20} \langle e|, \quad (4)$$

and the singlet and triplet t_c may, in principle, be different, especially when the excited state is determined by the valley degree of freedom. In this case, t_c^T/t_c^S is a function of the ‘‘valley mixing angle,’’ the rotation from one dot to the other of the relative phase between superpositions of the valley states [48,49].

For a given ϵ , H_S has an energy gap of $E(\epsilon, t_c) = \sqrt{\epsilon^2 + 4t_c^2}$, and its ground state has (2,0) population $P_{20} = [1 + \epsilon/E(\epsilon, t_c)]/2$. At finite temperature T_e , we find the system in its excited state with probability $\exp[-E(\epsilon, t_c)/k_B T_e]$. Weighting P_{20} by this value we obtain

$$P_{20}(\epsilon, t_c) = \frac{1}{2} + \frac{1}{2} \frac{\epsilon}{E(\epsilon, t_c)} \tanh \left[\frac{E(\epsilon, t_c)}{2k_B T_e} \right]. \quad (5)$$

H_T is identical up to an offset in ϵ and potentially a different tunnel coupling, allowing this form to be applied to both the singlet and triplet branches.

B. Fit function

To standardize the extraction of Δ_{SB} , we fit the intensity z measured as a function of binned current and detuning [Fig. 4(b)] to a functional form that combines the charge distribution from Eq. (5) with a model of the charge sensor's response. Assuming this response is linear in P_{20} , the probability of measuring current I at a given ϵ and t_c is proportional to

$$f(\epsilon, I, t_c) = \exp \left\{ -\frac{1}{2\sigma_I^2} [I - I_{\text{amp}} \times P_{20}(\epsilon, t_c)]^2 \right\}, \quad (6)$$

where I_{amp} is the signal contrast and σ_I is the current broadening.

Summing two of these distributions—one each for the spin-singlet and spin-triplet branches—and adding an overall current offset gives our final fit function,

$$z(\Delta_{SB}) = P_S \times f[\epsilon - \epsilon^0, I - (I^0 + m\epsilon), t_c^S] + P_T \times f[\epsilon - \epsilon^0 - \Delta_{SB}, I - (I^0 + m\epsilon), t_c^T], \quad (7)$$

where P_S and P_T are the relative populations of ground singlet and ground triplet with tunnel couplings t_c^S and t_c^T , respectively. ϵ is the dot-to-dot detuning in units of energy, and ϵ^0 is the detuning energy of the spin-singlet charge transition. I is the differential current through dot M, with constant offset I^0 and linear offset $m\epsilon$; the slope m stems from a linear cross capacitance between dots P_1/P_2 and dot M.

While these formulae provide a concrete fit model, the splitting extracted from this technique is largely independent of model details. The midpoint of each branch indicates the electrons' wave function is in an equal superposition of charge states, i.e., at an anticrossing. As long as this assumption holds, the distance between anticrossings gives Δ_{SB} (with no upper bound), regardless of higher-lying excited states, charge noise, or other effects that might distort the curves. By contrast, other parameters of Eq. (7), in particular t_c and T_e , are much more sensitive to the precise fit model (see Appendix). Although these model parameters give insight into the physics responsible for the measured lineshapes, in practice they only capture the slopes of the curves.

C. Fitting small splittings

In the case where the two branches are well separated, the energy-referred width of the SCC region in Fig. 4(a) serves as a reasonably good estimate of Δ_{SB} , up to corrections of order t_c . However, when SCC is not as robust, our technique is still effective at extracting Δ_{SB} . Figure 4(d) shows data, taken from a similar device, in which the branches are not visibly distinct. Though the horizontal separation between branches only manifests as a widening of the combined curve near the anticrossings, we are still able to extract Δ_{SB} . To bound our confidence in such a fit, we consider the extreme case of trying to determine Δ_{SB} from a single histogram [i.e., a vertical slice of a plot like Fig. 4(d)]. Using Eq. (5) we can relate Δ_{SB} to the separation of the histogram peaks, $\eta \equiv I_{\text{amp}} \{P_{20}[(\Delta_{SB}/2), t_c] - P_{20}[-(\Delta_{SB}/2), t_c]\}$. Specifically, by linearizing η about the anticrossing, we find

$$\eta \approx \frac{I_{\text{amp}}}{2t_c} \tanh \left(\frac{t_c}{k_B T_e} \right) \Delta_{SB} \equiv \lambda \Delta_{SB}, \quad (8)$$

where we introduce the slope λ to condense notation. Even at low splitting λ can be fit to high precision, so finding Δ_{SB} reduces to a problem of fitting the separation between mixed Gaussian distributions with finite statistics.

If the singlet and triplet histograms have variance σ_I^2 and means separated by η , the combined histogram's total variance is given by

$$\sigma_{\text{tot}}^2 = \sigma_I^2 + P_S P_T \eta^2. \quad (9)$$

If σ_I^2 is known to high precision, our uncertainty in η is limited by our uncertainty in σ_{tot} . After N measurements, we can find an approximate $\tilde{\sigma}_{\text{tot}}^2$, which bounds the actual σ_{tot}^2 according to

$$\tilde{\sigma}_{\text{tot}}^2 = \sigma_{\text{tot}}^2 \left[1 \pm \frac{2\text{erf}^{-1}(C)}{\sqrt{N}} \right], \quad (10)$$

where erf^{-1} is the inverse error function and C is the confidence of the estimate [e.g., $\text{erf}^{-1}(.95) \approx 1.39$ for 95% confidence]. Writing versions of Eq. (9) for both actual and estimated variables and plugging the results into Eq. (10), we find a relation between the actual η and estimated $\tilde{\eta}$, which simplifies to

$$\tilde{\eta} = \eta \sqrt{1 \pm \frac{2\text{erf}^{-1}(C)}{\sqrt{N}} \left(1 + \frac{\sigma_I^2}{\eta^2 P_S P_T} \right)}. \quad (11)$$

The first error term is the standard error in estimating the width of a distribution, while the second represents the added difficulty of measuring a separation between mixed Gaussians that is small compared to their individual variances. The latter implies N must scale with $(\sigma_I/\eta)^4$ to maintain a fixed uncertainty; this determines the minimum η that can be extracted with a reasonable number of measurements.

If the uncertainty in Eq. (11) is not overly large, we may wish to combine this with uncertainty in the other fit parameters to bound our overall confidence in Δ_{SB} . Let δX denote our fractional uncertainty in parameter X , i.e., $\tilde{X} = X(1 \pm \delta X)$. Equation (10) can be understood as an expression of $\delta\sigma_{\text{tot}}$. Expanding Eqs. (8) and (9) to first order in each δ , and assuming that errors add quadratically, we find

$$\delta\Delta_{\text{SB}}^2 \lesssim \delta\eta^2 + \delta\lambda^2, \quad (12)$$

$$\delta\eta^2 \approx \left[\frac{\text{erf}^{-1}(C)}{\sqrt{N}} \left(1 + \frac{\sigma_I^2}{\eta^2 P_S P_T} \right) \right]^2 + \left(\frac{|P_S - P_T|}{2P_T} \delta P_S \right)^2 + \left(\frac{\sigma_I^2}{\eta^2 P_S P_T} \delta\sigma_I \right)^2. \quad (13)$$

$\delta\lambda$ can be expanded into a function of δt_c , δI_{amp} , and δT_e , but these are generally correlated fit parameters whose errors may not add independently, so we express their

uncertainty collectively. As noted above, parameters other than Δ_{SB} can usually be fit to high precision, so the first term of Eq. (13), is the dominant source of uncertainty for small Δ_{SB} . If Δ_{SB} is large enough to resolve the singlet and triplet branches, the fit is determined by horizontal distance rather than histogram width, and uncertainty is instead dominated by our measurement of the lever arm, as described in Sec. II C.

Though the splitting from the fit shown in Fig. 4(d) ($\Delta_{\text{SB}} = 28.1 \mu\text{eV}$) is comparable to both the tunnel coupling ($t_c = 40.5 \mu\text{eV}$) and thermal broadening ($k_B T_e = 8.6 \mu\text{eV}$), Eq. (11) gives an uncertainty of approximately $2.5 \mu\text{eV}$ due to histogram width (with 95% confidence). Note that in practice, we never extract Δ_{SB} from a single histogram; fitting to the full dataset—including an estimate of η at each detuning—adds confidence to our estimate, so this uncertainty is an upper bound. Nonetheless, it shows that our technique can be used to measure splittings below $30 \mu\text{eV}$. This is especially valuable when investigating epitaxial methods to maximize Δ_{SB} , as accurate spectroscopy of attempts to control its magnitude may lend insight into the limiting mechanisms.

For dots with splittings greater than the tunnel coupling, the SNR of the singlet-triplet measurement is not fundamentally limited by t_c or T_e , but rather solely by σ_I and the current discrimination observed between the (1,1) and (2,0) charge states. Such is the case for dot $P1$, with an SNR of 6.5 near $\epsilon = \Delta_{\text{SB}}/2$ [shown in Fig. 4(c)]. This limit is apparent by noting that at the detuning indicated by the dashed green line of Fig. 4(b), the two branches are fully (1,1) and (2,0) in character. The measured current contrast is dictated by the capacitive coupling from dots $P1$ and $P2$ to the charge sensor, a property of this particular gate design. The uncertainty in the measured current, σ_I , of 7.6 pA is in excellent agreement with the calculated value of 7.7 pA obtained in Sec. II B.

IV. VARYING CONFINEMENT POTENTIAL

We now use this technique to measure how changes in confining potential affect Δ_{SB} of dots $P1$ and $P2$. Sweeping the bias voltages on gates $X1$ and $X2$ at a constant ratio, as indicated by the bottom and top axes of Fig. 5, deforms the confinement potentials while maintaining interdot tunnel couplings amenable to SCC. The data show the energy splittings for each dot decrease by a factor of approximately 2, with maximum values of approximately $150 \mu\text{eV}$ for Δ_{SB}^{P1} and approximately $80 \mu\text{eV}$ for Δ_{SB}^{P2} .

One effect which may give rise to this variation in Δ_{SB} with bias is a varying voltage-to-energy scaling caused by changes in cross capacitance or lever arm strength, α . We account for changes in cross capacitance by updating the values of $G_{P1,P2}$ and $G_{P2,P1}$ over the course of the sweep in Fig. 5. Although changes in the electrostatic potential can

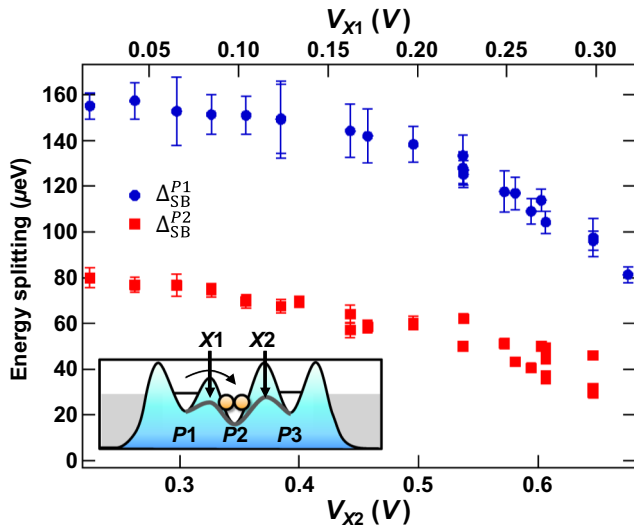


FIG. 5. Exchange gate modulation of two-electron excited-state energy. Measured ground-to-excited state energy separation of dots $P1$ (blue) and $P2$ (red) as a function of voltage applied to neighboring exchange gates. To maintain spin-to-charge conversion, each $X2$ voltage (bottom axis) is compensated with an $X1$ voltage (top axis). Error bars: uncertainty calculated from Eq. (11) for $C = 0.95$.

certainly affect α if the electron is localized far from under the center of the corresponding gate, we find this interpretation of the data to be inconsistent with our observations. Measurements of α from devices similar to the one studied here are typically performed in a low-exchange gate biasing regime (e.g., near the left-hand side of Fig. 5). By comparison, the measurements shown here are performed with the $X1$ and $X2$ exchange gates forward biased ($V_{X2} = 0.675$ V and $V_{X1} = 0.318$ V, right-hand side of Fig. 5). The agreement between typical values of lever arm strength (approximately 0.1 eV/V) with those measured here contrasts with the observed factor of 2 change in Δ_{SB} . Therefore, we conclude that the large tunability of Δ_{SB} is not confounded by significant changes in lever arm strength but that the underlying energy splitting is changing.

Identifying the physics responsible for this variation is important for improving device performance. The gradual, monotonic, and correlated change in Δ_{SB} over a wide range of biases suggests that valley splitting alone is not responsible: shifting electrons would sample disorder at the interface of a Si-Ge alloy in a more random fashion [21,33,50]. While plausible to have an arrangement of steps or changing vertical electric field that would simultaneously lower valley splitting in dots $P1$ and $P2$, a shift in the differential valley phase angle between electrons occupying the two dots [48,49,51] would likely be observed. However, the ratio of singlet and triplet tunnel couplings remains fairly constant in this experiment (see

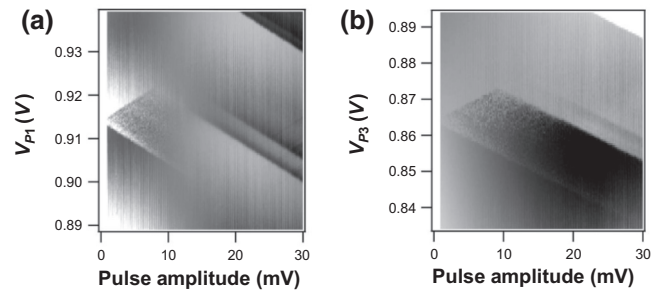


FIG. 6. Pulse-gate spectroscopy of single-electron loading. (a) Map of measured current through dot M as a function of the dc voltage, V_{P1} , and pulsed voltage amplitude applied to dot $P1$ near single-electron loading (approximately 0.915 V). Dot $P2$ is set approximately 20 mV below its single-electron loading voltage. (b) As in (a), but for dot $P3$ at single-electron loading (approximately 0.865 V). To improve clarity, a background current slope is subtracted from each dataset.

Appendix). We therefore posit that in this case, the most likely cause of the change in Δ_{SB} with bias is a modification of the two-electron orbital confinement, i.e., the quantum-dot confinement potential becomes more elliptical with forward bias on the barrier gates [16,19]. This is corroborated by our observations of significant asymmetry in single-electron orbital energies and calculations of the sensitivity of the two-electron orbital splitting to potential ellipticity.

A. Single-electron orbital asymmetry

Measurement of the lowest single-electron orbital excited-state energies is accomplished by pulse-gate spectroscopy [28,52,53]. We set the biases on $X1$ and $X2$ to the regime of low interdot coupling (left-hand side of Fig. 5), but with the middle dot, $P2$, unoccupied in order to avoid the occurrence of transitions from dots beyond the one being probed. We simultaneously sweep the dc voltage around the value at which dots $P1$ [Fig. 6(a)] and $P3$ [Fig. 6(b)] first load an electron while varying the amplitude of an approximately 700 kHz square wave pulse applied to the same gate. This reveals the first orbital excited-state energies in these dots, which for $P1$ are 1.623 and 2.13 meV and for $P3$ are 1.878 and 2.487 meV.

The fact that ellipticity in confining potentials can have a precipitous effect on two-electron singlet-triplet orbital splittings is well known [19], as demonstrated in Fig. 7. Employing a simple model of 2D parabolic potentials supporting our measured single-electron orbital energies, we find the orbital singlet-triplet splitting of two interacting electrons confined in silicon to be 198 μeV for dot $P1$ and 251 μeV for dot $P3$. This agrees reasonably well with the measured value of Δ_{SB}^{P1} , given the simplicity of the model—real potentials are more featured, which likely further reduces the singlet-triplet splitting—and the fact that these pulse-gate spectroscopy measurements cannot

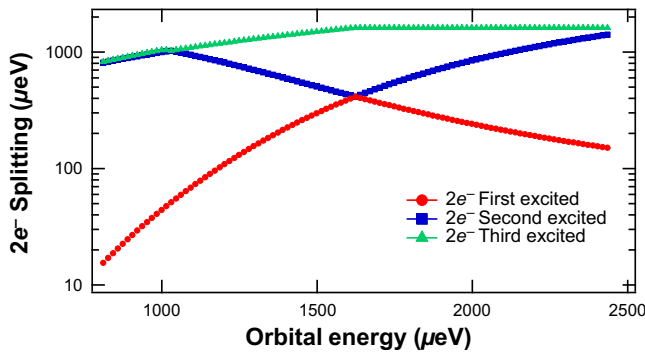


FIG. 7. Orbital splittings of two electrons confined in 2D parabolic potentials. One of the two lowest-lying orbital excited states of a single electron confined to the same potential is fixed at 1.623 meV, while the other varies along the horizontal axis. The point of degeneracy between the first and second excited states corresponds to a point of symmetry in the underlying confinement potential away from which the lowest-lying two-electron orbital excited state (singlet-triplet splitting) drops precipitously.

be performed at exactly the same biasing configurations explored by spin-blockade measurements. This interpretation is consistent with comparable singlet-triplet splittings (approximately 200 μeV) observed in GaAs quantum dots [54], a system lacking a valley degree of freedom, which have been shown to be gate tunable [55–57]. These observations highlight the necessity of considering both valley and orbital degrees of freedom when determining what limits the singlet-triplet energy splitting in Si quantum dots. We note that valley-orbit hybridization is possible and could be the cause of an apparent saturation in Δ_{SB} at tighter confinements [34]. The fact that two-electron orbital splittings are on par with expected valley splittings [22] and the delicate interplay between these two degrees of freedom necessitates an *in situ* measurement technique as described here.

V. CONCLUSION

We describe an excited-state spectroscopy method for measuring the two-electron ground-to-excited state energy separation of quantum dots. The extracted energy splitting is directly relevant to state preparation and measurement of singlet-triplet-based qubits. This technique, suitable when charge measurements are faster than spin T_1 , is applied to quantum dots tuned for spin-to-charge conversion. In showing the tunability of Δ_{SB} with confinement gate bias, we demonstrate the utility of this technique in optimizing device performance. It should be useful to any quantum-dot architecture that utilizes spin blockade.

ACKNOWLEDGMENTS

The authors gratefully acknowledge M. Gyure, D. Kim, T. Ladd, A. Pan, M. Reed, for helpful discussions.

APPENDIX: FITTING t_c

In addition to the two-electron ground-to-excited state splitting, Δ_{SB} , fitting data to Eq. (7) yields parameters describing the tunnel coupling, t_c . Due to the constancy of the ratio $t_c^S:t_c^T$ over the bias range examined, we report the tunnel coupling at each anticrossing as a single value here, t_c . The solid markers of Fig. 8 show t_c extracted from the data of Fig. 5, fit assuming a fixed value of T_e . This is contrasted with t_c extracted from the more established spin-funnel measurement technique, shown by open markers [58–60]. Notably, t_c extracted from spin-funnel measurements (which also consistently agree with Landau-Zener estimates of tunnel coupling, not shown here) are more than $10\times$ smaller than those estimated using spin-blockade fits. Even at the highest $X2$ voltages, where tunnel coupling dominates any temperature terms in the fit formula, the discrepancy persists. This suggests that this relatively simple, site-based coherent Fermi-Hubbard interaction model used to derive the fit functions in the main text is insufficient to describe tunnel coupling in real experiments.

The spin-funnel measurements of the (2,0)–(1,1) and (0,2)–(1,1) tunnel couplings shown in Fig. 8 are performed by measuring the location of the $S_0 - T_{\pm}$ avoided crossing as a function of applied magnetic field. This established measurement technique offers a reliable comparison for the tunnel coupling extracted other ways. The sequence employed first prepares a singlet state, biases near the

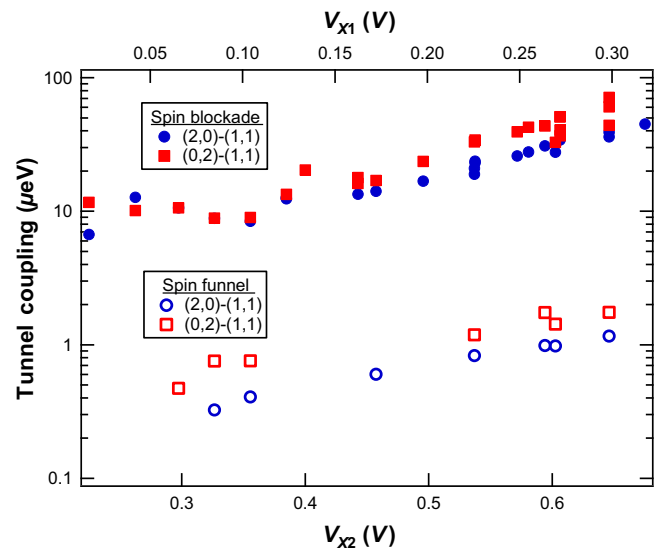


FIG. 8. Tunnel couplings extracted from spin-blockade fits compared to spin-funnel measurements. Tunnel coupling at the (2,0)–(1,1) anticrossing (blue) and (0,2)–(1,1) anticrossing (red), extracted from a Fermi-Hubbard model fit to single-shot data using fit functions in the main text at fixed T_e (solid markers) and tunnel couplings from spin-funnel measurements (open markers).

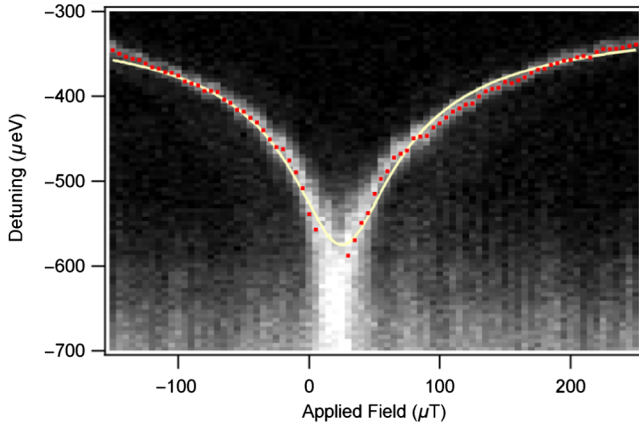


FIG. 9. Spin-funnel measurement of tunnel coupling. Grayscale contrast highlights the probability of measuring a Pauli-blockaded spin state as a function of detuning and applied magnetic field. Red markers denote extracted peak position for each column. The yellow line shows a fit to the red markers using Eq. (A1).

anticrossing of interest for a reference measurement, and then pulses to varying negative detunings [toward the (1,1) cell center] with a dwell time of $10 \mu\text{s}$, after which the final pulse returns to the spin-to-charge readout window for measurement. The $10 \mu\text{s}$ dwell time is chosen to be long enough to allow spin-orbit and hyperfine interactions to induce mixing between S_0 and T_{\pm} states at their anticrossing. This yields an increased probability of transitioning into the lower of the T_- and T_+ states at the detuning of that anticrossing (see Fig. 9).

The location of the $S_0 - T_{\pm}$ anticrossing is extracted by fitting a Gaussian profile to each column. The resulting peak location versus magnetic field is then fit to the functional form:

$$\varepsilon = y_0 - \frac{t_c^2}{g\mu_B \sqrt{(B - B_0)^2 + B_{\perp}^2}}, \quad (\text{A1})$$

from which we extract the tunnel coupling, $t_c = 1.07 \pm 0.02 \mu\text{eV}$, as well as the vertical ($B_0 = 25 \mu\text{T}$) and horizontal ($B_{\perp} = 36 \mu\text{T}$) offset fields.

As noted in the main text, while the Δ_{SB} extracted from spin-blockade fits is insensitive to our choice of model, t_c can be highly sensitive to model details. In particular, any effect that broadens the curves when fit to Eq. (7) leads to an overestimation of t_c , assuming that T_e has been reliably measured some other way. As a vivid example, we consider a process that dephases our system in the charge basis, possibly due to charge noise in ε or backaction from the measurement itself. We consider the density matrix describing our system, ρ , as it evolves under the coherent Hamiltonian H_S as well as Lindbladians describing thermalization and charge dephasing. Denoting the ground and

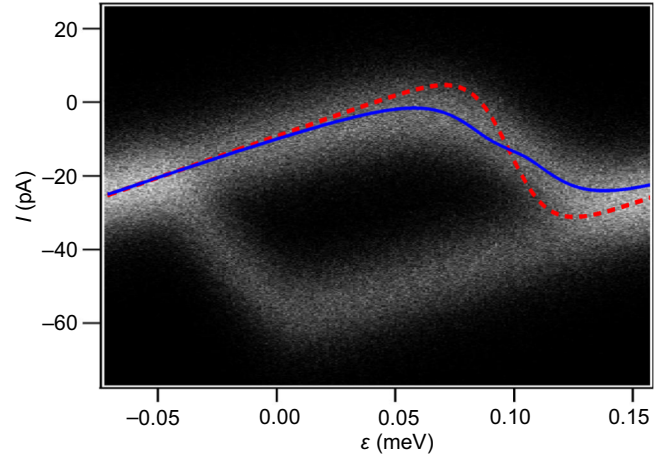


FIG. 10. Curve fits using t_c determined by spin funnel. With no charge dephasing (red dashed line), t_c is inadequate to match the observed broadening. With charge dephasing at $150\times$ the rate of thermalization (blue solid line), the broadening can be recovered.

excited eigenstates of H_S as $|-\rangle$ and $|+\rangle$ —not to be confused with the $|g\rangle_c$ and $|e\rangle_c$, the ground and excited states of a given charge configuration c —the master equation governing these dynamics is

$$\begin{aligned} \dot{\rho}(t) &= -i[H_S, \rho(t)] + \mathcal{L}_{\text{thermal}}[\rho(t)] + \mathcal{L}_{\text{charge}}[\rho(t)], \\ \mathcal{L}_{\text{thermal}}(\rho) &= -\gamma \left\{ \langle +|\rho|+ \rangle - \langle -|\rho|- \rangle \right. \\ &\quad \left. - \tanh\left[\frac{E(\varepsilon, t_c)}{2k_B T_e}\right] \right\} (|+\rangle \langle +| - |-\rangle \langle -|) \\ &\quad - \frac{\gamma}{2} (\langle +|\rho|- \rangle |+\rangle \langle -| + \text{h.c.}), \\ \mathcal{L}_{\text{charge}}(\rho) &= -\frac{\kappa}{2} ({}_{11}\langle g|\rho|g\rangle_{20} |g\rangle_{11} {}_{20}\langle g| + \text{h.c.}), \quad (\text{A2}) \end{aligned}$$

where γ and κ are the thermalization and charge-dephasing rates, respectively.

The quantity of interest in our measurement technique is the steady-state probability $P_{20}^{\text{ss}} \equiv \lim_{t \rightarrow \infty} P_{20}(t) = \lim_{t \rightarrow \infty} {}_{20}\langle g|\rho(t)|g\rangle_{20}$. Numerically, we find that charge dephasing can lead to large, multiplicative broadening of P_{20}^{ss} as a function of ε . The degree of broadening depends on κ/γ , i.e., the ratio of charge- to thermal-decoherence rates. If charge dephasing is much faster than thermalization, this can increase the extracted t_c by 2 orders of magnitude or more. This may explain the large discrepancy in values of t_c extracted from fitting Eq. (7) compared to those from spin-funnel measurements; a κ of approximately 150γ can resolve the discrepancy (see Fig. 10). However, including charge-state dephasing in the fit leaves T_e , t_c , κ , and γ as highly correlated parameters, and our fits are not sufficiently well resolved to distinguish them.

It is therefore too difficult to determine the impact of charge dephasing without an independent measurement of its magnitude, and so we mainly suggest it as an illustration of how broadening mechanisms can affect parameter estimation in our technique.

- [1] Thaddeus D. Ladd and Malcolm S. Carroll, in *Encyclopedia of Modern Optics (Second Edition)*, edited by Bob D. Guenther and Duncan G. Steel (Elsevier, Oxford, 2018), 2nd ed., p. 467.
- [2] Juha T. Muhonen, Juan P. Dehollain, Arne Laucht, Fay E. Hudson, Rachpon Kalra, Takeharu Sekiguchi, Kohei M. Itoh, David N. Jamieson, Jeffrey C. McCallum, Andrew S. Dzurak, and Andrea Morello, Storing quantum information for 30 seconds in a nanoelectronic device, *Nat. Nanotechnol.* **9**, 986 (2014).
- [3] Kevin Eng, Thaddeus D. Ladd, Aaron Smith, Matthew G. Borselli, Andrey A. Kiselev, Bryan H. Fong, Kevin S. Holabird, Thomas M. Hazard, Biqin Huang, Peter W. Deelman, Ivan Milosavljevic, Adele E. Schmitz, Richard S. Ross, Mark F. Gyure, and Andrew T. Hunter, Isotopically enhanced triple-quantum-dot qubit, *Sci. Adv.* **1**, e1500214 (2015).
- [4] Jun Yoneda, Kenta Takeda, Tomohiro Otsuka, Takashi Nakajima, Matthieu R. Delbecq, Giles Allison, Takumu Honda, Tetsuo Kodera, Shunri Oda, Yusuke Hoshi, Noritaka Usami, Kohei M. Itoh, and Seigo Tarucha, A quantum-dot spin qubit with coherence limited by charge noise and fidelity higher than 99.9%, *Nat. Nanotechnol.* **13**, 102 (2018).
- [5] M. D. Reed, B. M. Maune, R. W. Andrews, M. G. Borselli, K. Eng, M. P. Jura, A. A. Kiselev, T. D. Ladd, S. T. Merkel, I. Milosavljevic, E. J. Pritchett, M. T. Rakher, R. S. Ross, A. E. Schmitz, A. Smith, J. A. Wright, M. F. Gyure, and A. T. Hunter, Reduced Sensitivity to Charge Noise in Semiconductor Spin Qubits via Symmetric Operation, *Phys. Rev. Lett.* **116**, 110402 (2016).
- [6] Frederico Martins, Filip K. Malinowski, Peter D. Nissen, Edwin Barnes, Saeed Fallahi, Geoffrey C. Gardner, Michael J. Manfra, Charles M. Marcus, and Ferdinand Kuemmeth, Noise Suppression Using Symmetric Exchange Gates in Spin Qubits, *Phys. Rev. Lett.* **116**, 116801 (2016).
- [7] M. Veldhorst, J. C. C. Hwang, C. H. Yang, A. W. Leenstra, B. de Ronde, J. P. Dehollain, J. T. Muhonen, F. E. Hudson, K. M. Itoh, A. Morello, and A. S. Dzurak, An addressable quantum dot qubit with fault-tolerant control-fidelity, *Nat. Nanotechnol.* **9**, 981 EP (2014).
- [8] J. T. Muhonen, A. Laucht, S. Simmons, J. P. Dehollain, R. Kalra, F. E. Hudson, S. Freer, K. M. Itoh, D. N. Jamieson, J. C. McCallum, A. S. Dzurak, and A. Morello, Quantifying the quantum gate fidelity of single-atom spin qubits in silicon by randomized benchmarking, *J. Phys.: Condens. Matter* **27**, 154205 (2015).
- [9] M. A. Fogarty, K. W. Chan, B. Hensen, W. Huang, T. Tanttu, C. H. Yang, A. Laucht, M. Veldhorst, F. E. Hudson, K. M. Itoh, D. Culcer, A. Morello, and A. S. Dzurak, Integrated silicon qubit platform with single-spin addressability, exchange control and robust single-shot singlet-triplet readout, *Nat. Commun.* **9**, 4370 (2018).
- [10] Erika Kawakami, Thibaut Jullien, Pasquale Scarlino, Daniel R. Ward, Donald E. Savage, Max G. Lagally, Viatcheslav V. Dobrovitski, Mark Friesen, Susan N. Coppersmith, Mark A. Eriksson, and Lieven M. K. Vandersypen, Gate fidelity and coherence of an electron spin in an Si/SiGe quantum dot with micromagnet, *Proc. Natl. Acad. Sci.* **113**, 11738 (2016).
- [11] D. M. Zajac, A. J. Sigillito, M. Russ, F. Borjans, J. M. Taylor, G. Burkard, and J. R. Petta, Resonantly driven cnot gate for electron spins, *Science* **359**, 439 (2018).
- [12] C. H. Yang, K. W. Chan, R. Harper, W. Huang, T. Evans, J. C. C. Hwang, B. Hensen, A. Laucht, T. Tanttu, F. E. Hudson, S. T. Flammia, K. M. Itoh, A. Morello, S. D. Bartlett, and A. S. Dzurak, Silicon qubit fidelities approaching stochastic noise limits via pulse optimisation, arXiv:1807.09500 (2018).
- [13] W. Huang, C. H. Yang, K. W. Chan, T. Tanttu, B. Hensen, R. C. C. Leon, M. A. Fogarty, J. C. C. Hwang, F. E. Hudson, K. M. Itoh, A. Morello, A. Laucht, and A. S. Dzurak, Fidelity benchmarks for two-qubit gates in silicon, *Nature* **569**, 532 (2019).
- [14] M. Veldhorst, C. H. Yang, J. C. C. Hwang, W. Huang, J. P. Dehollain, J. T. Muhonen, S. Simmons, A. Laucht, F. E. Hudson, K. M. Itoh, A. Morello, and A. S. Dzurak, A two-qubit logic gate in silicon, *Nature* **526**, 410 (2015).
- [15] T. F. Watson, S. G. J. Philips, E. Kawakami, D. R. Ward, P. Scarlino, M. Veldhorst, D. E. Savage, M. G. Lagally, Mark Friesen, S. N. Coppersmith, M. A. Eriksson, and L. M. K. Vandersypen, A programmable two-qubit quantum processor in silicon, *Nature* **555**, 633 (2018).
- [16] R. Hanson, L. P. Kouwenhoven, J. R. Petta, S. Tarucha, and L. M. K. Vandersypen, Spins in few-electron quantum dots, *Rev. Mod. Phys.* **79**, 1217 (2007).
- [17] John King Gamble, Patrick Harvey-Collard, N. Tobias Jacobson, Andrew D. Baczewski, Erik Nielsen, Leon Maurer, Inès Montaña, Martin Rudolph, M. S. Carroll, C. H. Yang, A. Rossi, A. Rossi, A. S. Dzurak, and Richard P. Muller, Valley splitting of single-electron Si MOS quantum dots, *Appl. Phys. Lett.* **109**, 253101 (2016).
- [18] Timothy B. Boykin, Gerhard Klimeck, M. A. Eriksson, Mark Friesen, S. N. Coppersmith, Paul von Allmen, Fabiano Oyafuso, and Seungwon Lee, Valley splitting in strained silicon quantum wells, *Appl. Phys. Lett.* **84**, 115 (2004).
- [19] Dmitriy V. Melnikov and Jean-Pierre Leburton, Dimensionality effects in the two-electron system in circular and elliptic quantum dots, *Phys. Rev. B* **73**, 085320 (2006).
- [20] Kohei Sasaki, Ryuichi Masutomi, Kiyohiko Toyama, Kentarou Sawano, Yasuhiro Shiraki, and Tohru Okamoto, Well-width dependence of valley splitting in Si/SiGe quantum wells, *Appl. Phys. Lett.* **95**, 222109 (2009).
- [21] Lijun Zhang, Jun-Wei Luo, Andre Saraiva, Belita Koiller, and Alex Zunger, Genetic design of enhanced valley splitting towards a spin qubit in silicon, *Nat. Commun.* **4**, 2396 (2013).
- [22] Samuel F. Neyens, Ryan H. Foote, Brandur Thorgrimsson, T. J. Knapp, Thomas McJunkin, L. M. K. Vandersypen, Payam Amin, Nicole K. Thomas, James S. Clarke, D. E.

- Savage, M. G. Lagally, Mark Friesen, S. N. Coppersmith, and M. A. Eriksson, The critical role of substrate disorder in valley splitting in Si quantum wells, *Appl. Phys. Lett.* **112**, 243107 (2018).
- [23] W. G. van der Wiel, S. De Franceschi, J. M. Elzerman, T. Fujisawa, S. Tarucha, and L. P. Kouwenhoven, Electron transport through double quantum dots, *Rev. Mod. Phys.* **75**, 1 (2002).
- [24] X. Mi, Csaba G. Péterfalvi, Guido Burkard, and J. R. Petta, High-Resolution Valley Spectroscopy of Si Quantum Dots, *Phys. Rev. Lett.* **119**, 176803 (2017).
- [25] Joshua S. Schoenfeld, Blake M. Freeman, and Hong Wen Jiang, Coherent manipulation of valley states at multiple charge configurations of a silicon quantum dot device, *Nat. Commun.* **8**, 64 (2017).
- [26] W. H. Lim, C. H. Yang, F. A. Zwanenburg, and A. S. Dzurak, Spin filling of valley-orbit states in a silicon quantum dot, *Nanotechnology* **22**, 335704 (2011).
- [27] M. G. Borselli, K. Eng, E. T. Croke, B. M. Maune, B. Huang, R. S. Ross, A. A. Kiselev, P. W. Deelman, I. Alvarado-Rodriguez, A. E. Schmitz, M. Sokolich, K. S. Holabird, T. M. Hazard, M. F. Gyure, and A. T. Hunter, Pauli spin blockade in undoped Si/SiGe two-electron double quantum dots, *Appl. Phys. Lett.* **99**, 063109 (2011).
- [28] J. R. Prance, Zhan Shi, C. B. Simmons, D. E. Savage, M. G. Lagally, L. R. Schreiber, L. M. K. Vandersypen, Mark Friesen, Robert Joynt, and S. N. Coppersmith, *et al.*, Single-Shot Measurement of Triplet-Singlet Relaxation in a Si/SiGe Double Quantum Dot, *Phys. Rev. Lett.* **108**, 046808 (2012).
- [29] Takashi Nakajima, Matthieu R. Delbecq, Tomohiro Otsuka, Peter Stano, Shinichi Amaha, Jun Yoneda, Akito Noiri, Kento Kawasaki, Kenta Takeda, Giles Allison, Arne Ludwig, Andreas D. Wieck, Daniel Loss, and Seigo Tarucha, Robust Single-Shot Spin Measurement with 99.5% Fidelity in a Quantum Dot Array, *Phys. Rev. Lett.* **119**, 017701 (2017).
- [30] Patrick Harvey-Collard, Benjamin D'Anjou, Martin Rudolph, N. Tobias Jacobson, Jason Dominguez, Gregory A. Ten Eyck, Joel R. Wendt, Tammy Pluym, Michael P. Lilly, William A. Coish, Michel Pioro-Ladrière, and Malcolm S. Carroll, High-Fidelity Single-Shot Readout for a Spin Qubit via an Enhanced Latching Mechanism, *Phys. Rev. X* **8**, 021046 (2018).
- [31] G. Zheng, N. Samkharadze, M. L. Noordam, N. Kalhor, D. Brousse, A. Sammak, G. Scappucci, and L. M. K. Vandersypen, Rapid high-fidelity gate-based spin read-out in silicon, arXiv:1901.00687 (2019).
- [32] J. R. Petta, A. C. Johnson, A. Yacoby, C. M. Marcus, M. P. Hanson, and A. C. Gossard, Pulsed-gate measurements of the singlet-triplet relaxation time in a two-electron double quantum dot, *Phys. Rev. B* **72**, 161301 (2005).
- [33] Zhan Shi, C. B. Simmons, J. R. Prance, John King Gamble, Mark Friesen, D. E. Savage, M. G. Lagally, S. N. Coppersmith, and M. A. Eriksson, Tunable singlet-triplet splitting in a few-electron Si/SiGe quantum dot, *Appl. Phys. Lett.* **99**, 233108 (2011).
- [34] Mark Friesen and S. N. Coppersmith, Theory of valley-orbit coupling in a Si/SiGe quantum dot, *Phys. Rev. B* **81**, 115324 (2010).
- [35] C. H. Yang, A. Rossi, R. Ruskov, N. S. Lai, F. A. Mohiyaddin, S. Lee, C. Tahan, G. Klimeck, A. Morello, and A. S. Dzurak, Spin-valley lifetimes in a silicon quantum dot with tunable valley splitting, *Nat. Commun.* **4**, 2069 EP (2013).
- [36] N. S. Lai, W. H. Lim, C. H. Yang, F. A. Zwanenburg, W. A. Coish, F. Qassemi, A. Morello, and A. S. Dzurak, Pauli spin blockade in a highly tunable silicon double quantum dot, *Sci. Rep.* **1**, 110 (2011).
- [37] M. G. Borselli, K. Eng, R. S. Ross, T. M. Hazard, K. S. Holabird, B. Huang, A. A. Kiselev, P. W. Deelman, L. D. Warren, I. Milosavljevic, A. E. Schmitz, M. Sokolich, M. F. Gyure, and A. T. Hunter, Undoped accumulation-mode Si/SiGe quantum dots, *Nanotechnology* **26**, 375202 (2015).
- [38] D. M. Zajac, T. M. Hazard, X. Mi, K. Wang, and J. R. Petta, A reconfigurable gate architecture for Si/SiGe quantum dots, *Appl. Phys. Lett.* **106**, 223507 (2015).
- [39] Daniel R. Ward, Dohun Kim, Donald E. Savage, Max G. Lagally, Ryan H. Foote, Mark Friesen, Susan N. Coppersmith, and Mark A. Eriksson, State-conditional coherent charge qubit oscillations in a Si/SiGe quadruple quantum dot, *Npj Quantum Inf.* **2**, 16032 (2016).
- [40] S. A. Studenikin, L. Gaudreau, K. Kataoka, D. G. Austing, and A. S. Sachrajda, Enhancement-mode two-channel triple quantum dot from an undoped Si/Si_{0.8}Ge_{0.2} quantum well hetero-structure, *Appl. Phys. Lett.* **112**, 233101 (2018).
- [41] D. M. Zajac, T. M. Hazard, X. Mi, E. Nielsen, and J. R. Petta, Scalable Gate Architecture for a One-dimensional Array of Semiconductor Spin Qubits, *Phys. Rev. Appl.* **6**, 054013 (2016).
- [42] Peter W. Deelman, Lisa F. Edge, and Clayton A. Jackson, Metamorphic materials for quantum computing, *MRS Bull.* **41**, 224 (2016).
- [43] B. E. Kane, A silicon-based nuclear spin quantum computer, *Nature* **393**, 133 (1998).
- [44] I. T. Vink, T. Nooitgedagt, R. N. Schouten, L. M. K. Vandersypen, and W. Wegscheider, Cryogenic amplifier for fast real-time detection of single-electron tunneling, *Appl. Phys. Lett.* **91**, 123512 (2007).
- [45] T. H. Stoof and Yu. V. Nazarov, Time-dependent resonant tunneling via two discrete states, *Phys. Rev. B* **53**, 1050 (1996).
- [46] T. H. Oosterkamp, T. Fujisawa, W. G. van der Wiel, K. Ishibashi, R. V. Hijman, S. Tarucha, and L. P. Kouwenhoven, Microwave spectroscopy of a quantum-dot molecule, *Nature* **395**, 873 (1998).
- [47] L. Di Carlo, H. J. Lynch, A. C. Johnson, L. I. Childress, K. Crockett, C. M. Marcus, M. P. Hanson, and A. C. Gossard, Differential Charge Sensing and Charge Delocalization in a Tunable Double Quantum dot, *Phys. Rev. Lett.* **92**, 226801 (2004).
- [48] Dimitrie Culcer, Xuedong Hu, and S. Das Sarma, Interface roughness, valley-orbit coupling, and valley manipulation in quantum dots, *Phys. Rev. B* **82**, 205315 (2010).
- [49] M. L. V. Tagliaferri, P. L. Bavdaz, W. Huang, A. S. Dzurak, D. Culcer, and M. Veldhorst, Impact of valley phase and splitting on readout of silicon spin qubits, *Phys. Rev. B* **97**, 245412 (2018).

- [50] J. C. Abadillo-Uriel, B. Thorgrimsson, D. Kim, L. W. Smith, C. B. Simmons, D. R. Ward, R. H. Foote, J. Corrigan, D. E. Savage, M. G. Lagally, M. J. Calderón, S. N. Coppersmith, M. A. Eriksson, and M. Friesen, Signatures of atomic-scale structure in the energy dispersion and coherence of a Si quantum-dot qubit, *Phys. Rev. B* **98**, 165438 (2018).
- [51] Mark Friesen, Sucismita Chutia, Charles Tahan, and S. N. Coppersmith, Valley splitting theory of SiGe/Si/SiGe quantum wells, *Phys. Rev. B* **75**, 115318 (2007).
- [52] J. M. Elzerman, R. Hanson, L. H. Willems van Beveren, L. M. K. Vandersypen, and L. P. Kouwenhoven, Excited-state spectroscopy on a nearly closed quantum dot via charge detection, *Appl. Phys. Lett.* **84**, 4617 (2004).
- [53] C. B. Simmons, J. R. Prance, B. J. Van Bael, Teck Seng Koh, Zhan Shi, D. E. Savage, M. G. Lagally, R. Joynt, Mark Friesen, S. N. Coppersmith, and M. A. Eriksson, Tunable Spin Loading and T_1 of a Silicon Spin Qubit Measured by Single-shot Readout, *Phys. Rev. Lett.* **106**, 156804 (2011).
- [54] J. Medford, J. Beil, J. M. Taylor, S. D. Bartlett, A. C. Doherty, E. I. Rashba, D. P. DiVincenzo, H. Lu, A. C. Gossard, and C. M. Marcus, Self-consistent measurement and state tomography of an exchange-only spin qubit, *Nat Nano* **8**, 654 (2013).
- [55] Jordan Kyriakidis, M. Pioro-Ladriere, M. Ciorga, A. S. Sachrajda, and P. Hawrylak, Voltage-tunable singlet-triplet transition in lateral quantum dots, *Phys. Rev. B* **66**, 035320 (2002).
- [56] D. M. Zumbühl, C. M. Marcus, M. P. Hanson, and A. C. Gossard, Cotunneling Spectroscopy in Few-electron Quantum Dots, *Phys. Rev. Lett.* **93**, 256801 (2004).
- [57] A. C. Johnson, J. R. Petta, C. M. Marcus, M. P. Hanson, and A. C. Gossard, Singlet-triplet spin blockade and charge sensing in a few-electron double quantum dot, *Phys. Rev. B* **72**, 165308 (2005).
- [58] J. R. Petta, A. C. Johnson, J. M. Taylor, E. A. Laird, A. Yacoby, M. D. Lukin, C. M. Marcus, M. P. Hanson, and A. C. Gossard, Coherent manipulation of coupled electron spins in semiconductor quantum dots, *Science* **309**, 2180 (2005).
- [59] J. R. Petta, J. M. Taylor, A. C. Johnson, A. Yacoby, M. D. Lukin, C. M. Marcus, M. P. Hanson, and A. C. Gossard, Dynamic Nuclear Polarization with Single Electron Spins, *Phys. Rev. Lett.* **100**, 067601 (2008).
- [60] B. M. Maune, M. G. Borselli, B. Huang, T. D. Ladd, P. W. Deelman, K. S. Holabird, A. A. Kiselev, I. Alvarado-Rodriguez, R. S. Ross, A. E. Schmitz, M. Sokolich, C. A. Watson, M. F. Gyure, and A. T. Hunter, Coherent singlet-triplet oscillations in a silicon-based double quantum dot, *Nature* **481**, 344 (2012).